High plating currents without dendrites at the lithium anode/solid electrolyte interface

Dominic L. R. Melvin[1], Marco Siniscalchi[1], Dominic Spencer-Jolly[1,2], Bingkun Hu[1], Ziyang Ning[1], Shengming Zhang[1], Junfu Bu[1], Shashidhara Marathe[3], Anne Bonnin[4], Johannes Ihli[1,4], Gregory J. Rees[1], Patrick S. Grant[1], T. James Marrow[1], Guanchen Li[5], Peter G. Bruce[1,6]*

1. Department of Materials, University of Oxford, Oxford, UK

2. School of Metallurgy and Materials, University of Birmingham, Pritchatts Road, Birmingham, UK

3. Diamond Light Source, Harwell Campus, Didcot, UK

4. Paul Scherrer Institut, Villigen, Switzerland.

5. James Watt School of Engineering, University of Glasgow, Glasgow, UK

6. Department of Chemistry, University of Oxford, Oxford, UK

*Correspondence: peter.bruce@materials.ox.ac.uk

Abstract

Avoiding lithium dendrites at the lithium/ceramic electrolyte interface and as a result avoiding cell short-circuit when plating at practical current densities remains a significant challenge for all-solid-state batteries. Typically, values are limited to around 1 mA cm^{-2}, even, for example, for garnets with a relative density of >99%. It is not obvious that simply densifying ceramic electrolytes will deliver high plating currents. Here we show that plating currents of 9 mA cm^{-2} can be achieved without dendrite formation, by densifying Argyrodite, Li_6PS_5Cl, to 99%. Changes in the microstructure of Li_6PS_5Cl on densification from 83 to 99% were determined by FIB-SEM tomography and used to calculate their effect on the critical current density (CCD). Not all changes in microstructure with densification act to increase CCD. While smaller pores and shorter cracks increase CCD, lower pore population and narrower cracks act to decrease CCD. Calculations show that the former changes dominate over the latter, predicating an overall increase in CCD, as observed experimentally.

Introduction

All-solid-state batteries based on a lithium metal anode and ceramic electrolyte have the potential to achieve high energy densities[1–3]. Avoiding lithium dendrites (filaments of lithium) that penetrate the solid electrolyte (SE) on charging (lithium plating) leading ultimately to a short-circuit at practical current densities remains a significant challenge[4–22]. The need for fast charging, in for example electric vehicles, means that plating current densities in excess of 5 mA cm^{-2} are desirable[23,24]. The major classes of solid electrolyte under consideration, LLZO, sulphides and halides, struggle to achieve lithium plating currents in this range without dendrite penetration, short-circuit and cell failure[25–29]. For example, extensive work on garnets, including LLZO, have shown that plating currents are typically limited to around 1 mA cm^{-2} even when the electrolyte is 99% dense or above, calling into question whether densifying polycrystalline ceramic electrolytes can achieve high plating currents[30–32].

1

Work to address the challenge of avoiding dendrites at high plating currents (high CCD) has explored altering the Li/SE interface or modifying the solid electrolyte. At the Li/SE interface, notable strategies have included the addition of a thin interlayer as well as patterning of the solid electrolyte surface[33–46]. Regarding the solid electrolyte, the addition of composite phases, bilayered electrolytes and the use of single crystals have all been explored[30,47–52]. An important study by Krauskopf *et al.*[53] has demonstrated that high plating currents can be obtained at microelectrodes placed within grains, i.e. in defect free regions, yet such currents remain elusive when using bulk Li anodes. In an attempt to avoid grain boundaries, glasses have been investigated[51,54–57]. However, generally, glasses are found to be brittle, and despite avoiding grain boundaries, limiting imperfections may still remain[54,58]. It has been reported that thin-film batteries based on LiPON can avoid dendrites when charged at fast rates, but their low conductivity means that they are not suitable for larger cells[59,60].

Recent modelling studies have shown high plating currents should occur when the microstructure of a polycrystalline solid electrolyte has small pores that are close together and cracks that are short and wide[12]. However, not all of these microstructural parameters are expected to improve on densification, therefore it is not obvious that densification will deliver high CCDs. Sulphide based solid electrolytes have the highest conductivity and have therefore received considerable attention as possible solid electrolytes for solid-state batteries[61]. Argyrodite, Li_6PS_5Cl, has a high conductivity and although it reacts with lithium metal, it does so to form a solid electrolyte interphase that stabilises, mitigating further reactivity[62]. Here we investigate the effect of densification on the Li_6PS_5Cl microstructure and CCD. We show that plating currents as high as 9 mA cm^{-2} can be achieved without lithium dendrites (and as a consequence without short-circuit) by densifying the solid electrolyte to 99%. Extracting the changes in the microstructure on densification from FIB-SEM tomography and then using the changes in the microstructural dimensions to calculate CCD shows that the smaller pores and shorter cracks that occur on densification act to increase CCD, whereas narrower cracks and greater distance between pores (lower population density) act to reduce CCD. Therefore, not all the changes in the microstructure of Li_6PS_5Cl upon densification act to increase CCD. The calculations show that the reduction in pore size and the shorter crack lengths outweigh the narrower cracks and lower population density, predicting higher CCDs overall with densification, which is confirmed by experiment. These high plating currents avoiding dendrites are achieved without the need to form alloys with lithium, without the need to modify the solid electrolyte surface or to introduce interlayers.

Results and discussion

Li_6PS_5Cl polycrystalline solid electrolytes with a range of densities from 83% to 99% were prepared by sintering under different conditions. Powder X-ray diffraction patterns confirming the single-phase nature of the Argyrodite after sintering are shown in Fig S1. 3-electrode cells were assembled with Li metal working and counter electrodes (see Methods). The critical currents at which dendrites form (CCD) for the solid electrolytes of different density are shown in Fig 1, along with 3D reconstructed microstructures obtained by FIB-SEM serial sectioning and imaging, and FIB-SEM cross-sections. The CCD increases from 1 mA cm^{-2} for the 83% dense solid electrolyte to 10 mA cm^{-2} for the material with 99% relative density. The CCD results are supported by the micro X-ray computed tomography (XCT) data in Fig 2 and discussed below, which show no dendritic cracks in the 99% dense solid electrolyte at 9 mA cm^{-2} but a dendrite at 10 mA cm^{-2}. The lowest density solid electrolyte was formed by cold pressing the powder, which is the most widely used method for forming sulphide solid electrolytes[5,63,64]. Higher densities were achieved by spark plasma sintering. The process

2

involves passing a current through the die and solid electrolyte disc resulting in more homogeneous and rapid heating than conventional methods. Densities of 86, 95 and 99% were obtained by heating respectively at 300, 350 and 400 ºC for 5 mins. CCDs were determined as described in Methods (see also Fig S2), which also contains more details of the sintering. Densities were determined by weighing the discs and establishing the volume of the electrolyte from XCT measurements.
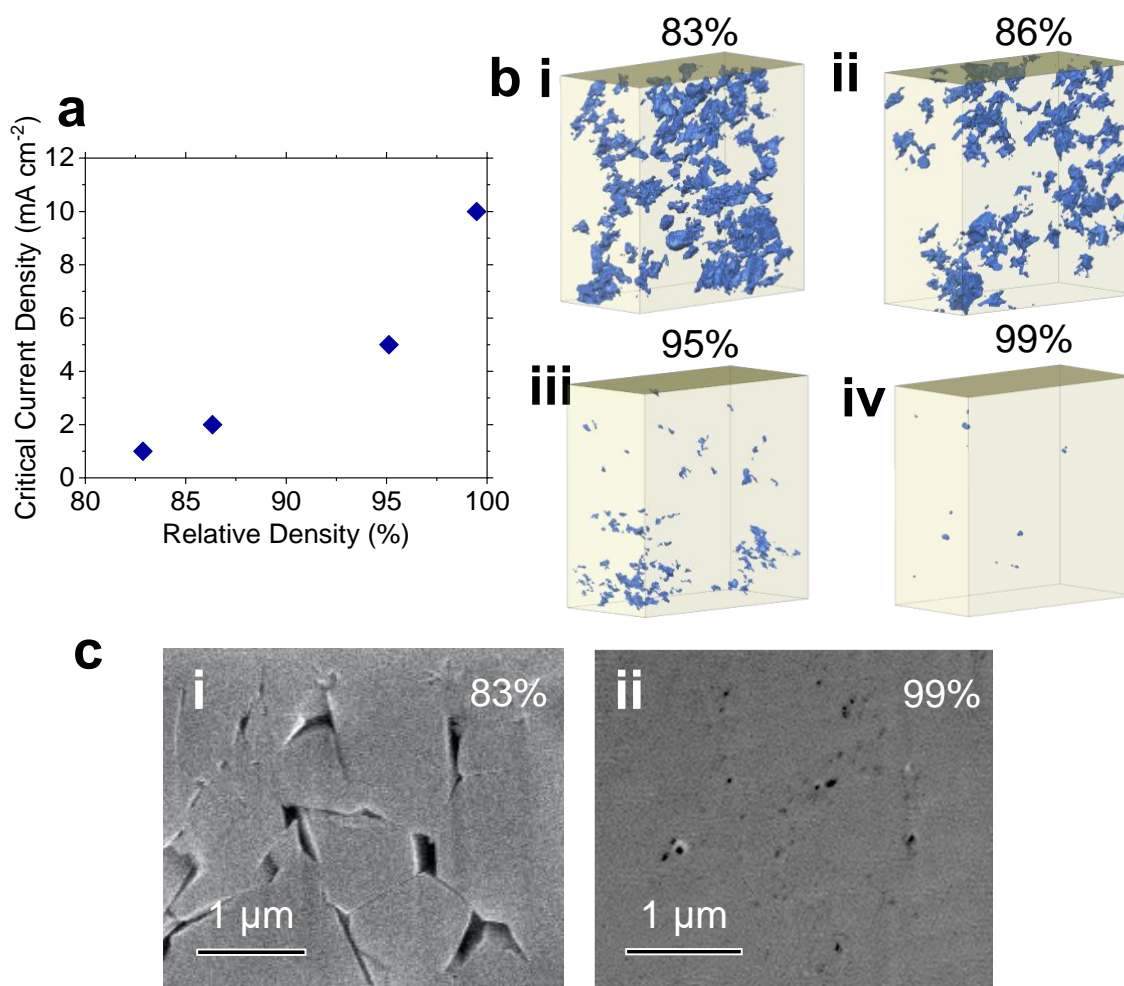

Figure 1. Critical currents for dendrite formation along with 3D reconstructions and FIB-SEM cross-sectional images of the microstructure showing the extent to which CCDs increase with densification. a. Critical current density for dendrite formation vs. relative density of Li_6PS_5Cl solid electrolytes densified under different conditions: 83% (cold pressed), 86, 95 and 99% spark plasma sintered at 300, 350 and 400°C for 5 mins. **b.** 3D reconstructed microstructures of Li_6PS_5Cl solid electrolytes for the differently densified solid electrolytes in **a.** 3D microstructures obtained using FIB-SEM serial sectioning and imaging. Regions of porosity are coloured blue. **c. i** and **ii** are magnified FIB-SEM cross-sections of the 83 and 99% dense solid electrolytes in **bi** and **biv**.

The microstructure changes significantly between 83 and 99% dense solid electrolytes. The 3D reconstructions, Fig 1b, show that the porosity decreases markedly with increasing densification. The SEM images in Fig 1c show the presence of grains in the 83% dense material whereas the 99% material exhibits greater homogeneity, it is harder to identify individual grains. Sulphides are mechanically soft. Their Young's moduli are typically in the range 10-30 GPa[12,58,65,66] compared with oxides of 150-200 GPa[67–69]. Conventional thinking

based on oxide ceramics may not be the best approach to understand these compliant materials, which densify to some extend even with cold pressing and to a very significant extent when heated at relatively low temperatures (several hundred degrees) for short durations.
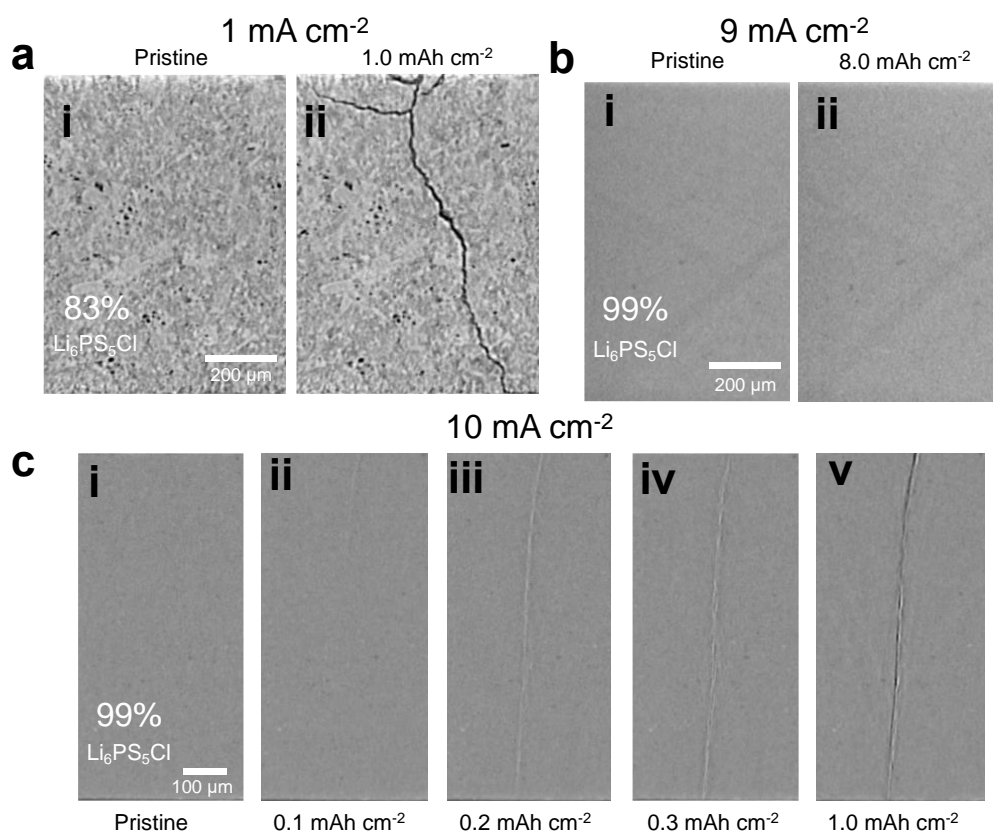

Figure 2. In-situ XCT virtual cross-sections during plating at the Li/Li$_6$PS$_5$Cl interface of Li/Li$_6$PS$_5$Cl/Li cells for high and low density Li$_6$PS$_5$Cl solid electrolytes demonstrating dendrite cracks form at the CCD but not below. Virtual XCT cross-sections of Li/Li$_6$PS$_5$Cl/Li cells with plating at the top electrode **a.** for a cold pressed Li$_6$PS$_5$Cl electrolyte (83% dense) **i** pristine and **ii** after plating 1 mAh cm^{-2} at 1 mA cm^{-2}. **b.** for a 400°C sintered Li$_6$PS$_5$Cl electrolyte (99% dense) **i** pristine and **ii** after plating 8 mAh cm^{-2} at 9 mA cm^{-2}. **c.** same dense electrolyte with plating at 10 mA cm^{-2} **i** pristine, **ii** after plating 0.1 mAh cm^{-2} **iii** 0.2 mAh cm^{-2} **iv** 0.3 mAh cm^{-2} **v** 1 mAh cm^{-2}. The Li electrodes have been removed from the images for clarity.

While the CCD measurements indicate that densifying the electrolyte suppresses dendrites and as a consequence short-circuits, it is instructive to examine with XCT what happens when lithium is plated. XCT virtual cross sections are presented in Fig 2. The data were collected from symmetric two electrode cells with lithium being plated at the electrode at the top of the images. The lithium electrodes have been removed from the XCT for clarity. Fig 2a shows the virtual cross section of the cell with the 83% dense solid electrolyte before and after plating a capacity of 1 mAh cm^{-2} at a rate of 1 mA cm^{-2}. The image after plating is very similar to those reported previously for lower density Argyrodite[12,13], with a spalled-out piece of the ceramic and the transverse crack reaching the other electrode. The current density at which this occurs is also consistent with previous work[12,13,25]. In contrast, the cell with the 99% solid electrolyte plated at a current density of 9 mA cm^{-2} shows no evidence of a dendritic crack, Fig 2b. This is also demonstrated in the 3D reconstructions of the XCT data in Figure S3. Repeating the experiment on the 99% dense solid electrolyte but increasing the current density to 10 mA cm^{-2} does result in a dendritic crack, Fig 2c and Figure S3. The cracks are however different

4

between the low and high-density ceramics. In the case of the dense solid electrolyte there is no evidence of spallation, and the transverse crack follows a very straight path to the other electrode. The XCT virtual cross-sectional images in Figure 2b&c for 99% dense solid electrolytes confirm that the CCD is between 9 and 10 mA cm^{-2}, in accord with the electrochemical measurements in Fig 1.

The experimental results in Figures 1 and 2 show that sintering changes the Li$_6$PS$_5$Cl solid electrolyte microstructure and increases CCD. However, are the changes in microstructure with densification responsible for the high CCD? To explore how the changes in microstructure influence CCD, we need to extract the dimensions of the microstructure (pores and cracks) and how they change on densification, then use these to calculate the CCDs. For the latter we employ the recently published model of dendrite penetration into polycrystalline ceramic electrolytes[12]. The dendrite model is based on the viscoplastic flow of lithium. On plating, Li deposits and grows along cracks in the ceramic from the anode to fill sub-surface pores. If the current density is sufficiently high that the Li being plated into the pores exceeds the Li flow out to the extent that pressure in the pores exceeds the local fracture strength at the grain boundaries, then a dendritic crack initiates. The CCDs for crack initiation depend on the pore size and population density (pore proximity) as well as the length and width of cracks connecting the pores to the interface[12]. More details of the model can be found in the supplementary information and Fig S4.
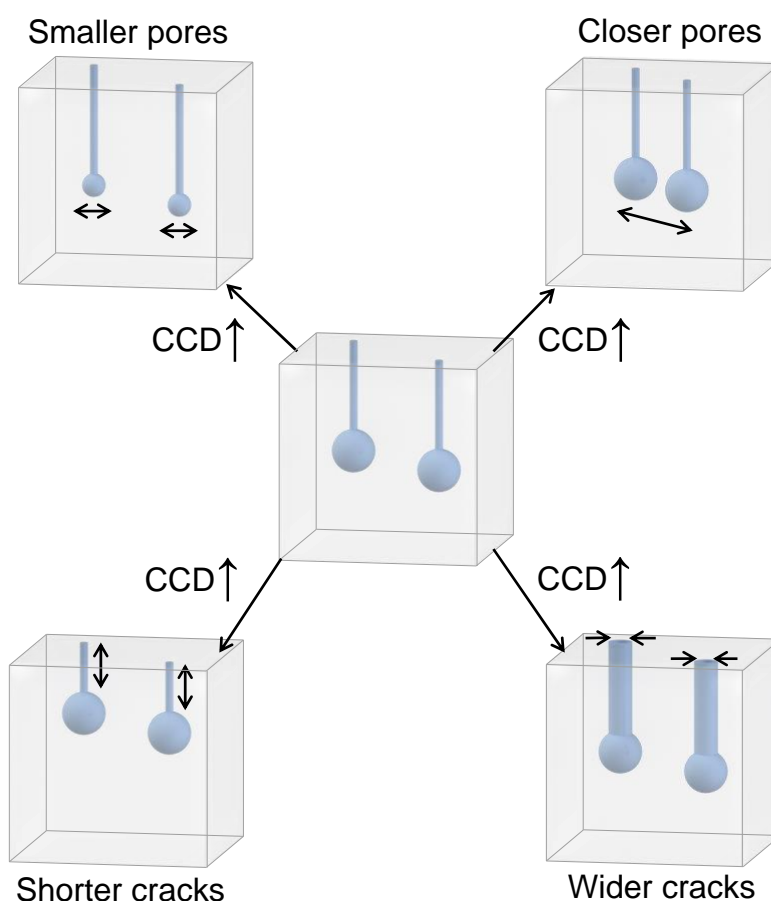

Figure 3. Schematic demonstrating key parameters affecting dendrite initiation. Reduction in pore size and pore separation, shorter and wider cracks lead to an increase in the critical current density.

The dimensions of the microstructure pores and cracks for each of the densified Li_6PS_5Cl solid electrolytes were determined by analysing the FIB-SEM tomographic images from the near surface region of each electrolyte, providing a resolution (~40 nm) below the limit typically available from XCT measurements. The method involves imaging a series of FIB-SEM sections allowing reconstruction of a 3D volume which can be analysed. How the dimensions were obtained from the imaging for each microstructure is described further in the Methods. The microstructure of a polycrystalline ceramic contains a distribution of pore and crack sizes. Our previous work showed that it is the large pores within the distribution of pore sizes that are primarily responsible for dendrite formation[12]. They are the weakest points as their larger surface area results in greater influx of lithium, hence greater pressure in the pore for a given overall current density. Considering the differently densified solid electrolytes, the largest pores range from 0.5 (high density) to 2.3 μm (low density) in radii. The current at a given pore is affected by the size and proximity of the neighbouring pores[12]. The neighbouring pores spread the current reducing it at a given pore, Fig S5. The effect drops off rapidly with the size of the neighbouring pores. We have modelled here how the current at a given pore is dependent on the size of neighbouring pores and this shows that only for pore sizes within a radius of 1/3 of the pore in question is the effect significant. For pores less than 1/3 of the size the effect is < 10%, see Fig S5. Therefore, we consider only neighbouring pores within 1/3 of the radius of the largest pores. The range of pore proximity with radii within 1/3 of the largest is 10 (low density) to 22 μm (high density). The pore sizes and proximities from the microstructural analysis were used to define the ranges shown in Fig 4a. Pores very close to the surface cannot build pressures to crack the ceramic as extrusion is too fast (easy), also the modelling shows deeper pores attract more current and so will build greater pressure, Fig S6. Therefore, we consider the longer cracks (deeper pores) for each density and their associated widths. The longest cracks measured within the differently densified solid electrolytes were found to range from 2.5 (low density) to 1.5 μm (high density). The average widths of the longest cracks (within 33% of the longest cracks) within each electrolyte was found to vary from 158 (low density) to 125 nm (high density). The crack lengths and widths were used to define the ranges in Fig 4b.
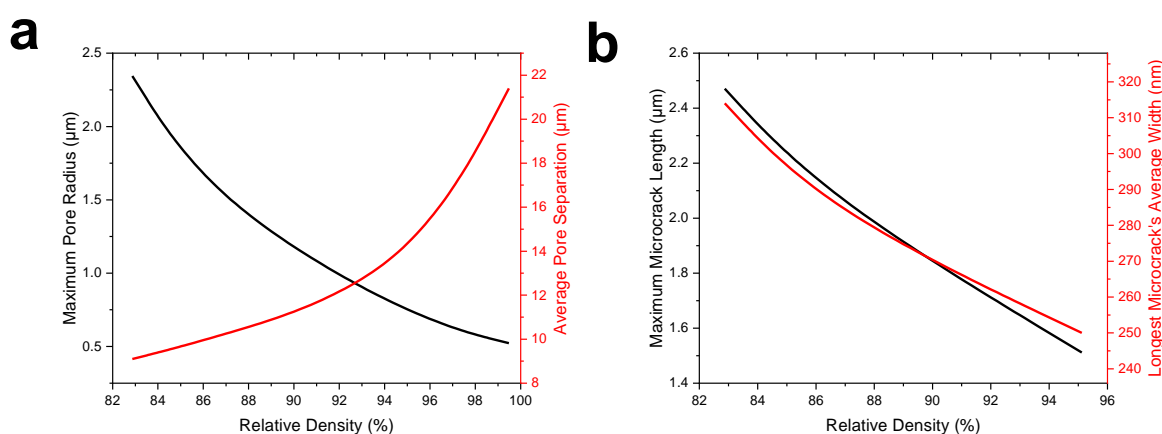

Figure 4. Plots of how pore and crack dimensions vary with density of Li_6PS_5Cl constructed using values from FIB-SEM tomography a the largest pore size and their average separation. **b** the maximum crack length and their associated width.

Fig 5a-d illustrates how CCD varies with pore size and separation as well as crack length and width. The ranges of the microstructure dimensions used in Fig 5 are obtained from Fig 4, and thus represent typical values expected when densifying Li_6PS_5Cl. Looking at Fig 5a&b, CCD decreases with increasing pore size and separation, both due to their effect on the magnitude

of current experienced by a given pore. As shown in Fig 5c&d, CCD increases with increasing crack width and decreases with increasing crack length, both due to the effect of width and length on the rate of Li extrusion. The dependence of CCD on a wider range of microstructural dimensions is shown in Fig S7&8, but the trends are the same as in Fig 5. Figure 4 shows that densifying Li_6PS_5Cl results in shorter and narrower cracks as well as smaller pores with greater separation. Therefore, not all changes in microstructure during the densification of Li_6PS_5Cl act to increase CCD. While decreasing crack width and increasing pore separation acts to decrease CCD, at the same time the decreasing crack length and pore size act to increase it. The calculations show, Figure 5e, that the former outweigh the latter predicting an overall increase in CCD as observed experimentally, Fig 1. While the trends in the predicted and experimental CCDs are the same, Figures 1a and 5e, we do not expect a close match between the absolute values; for example, even the larger pores for a given density are not of identical size. Also, the microstructure model assumes a simple geometry for pores (spheres) and cracks (cylinders) whereas actual pores and cracks will have more complex shapes.
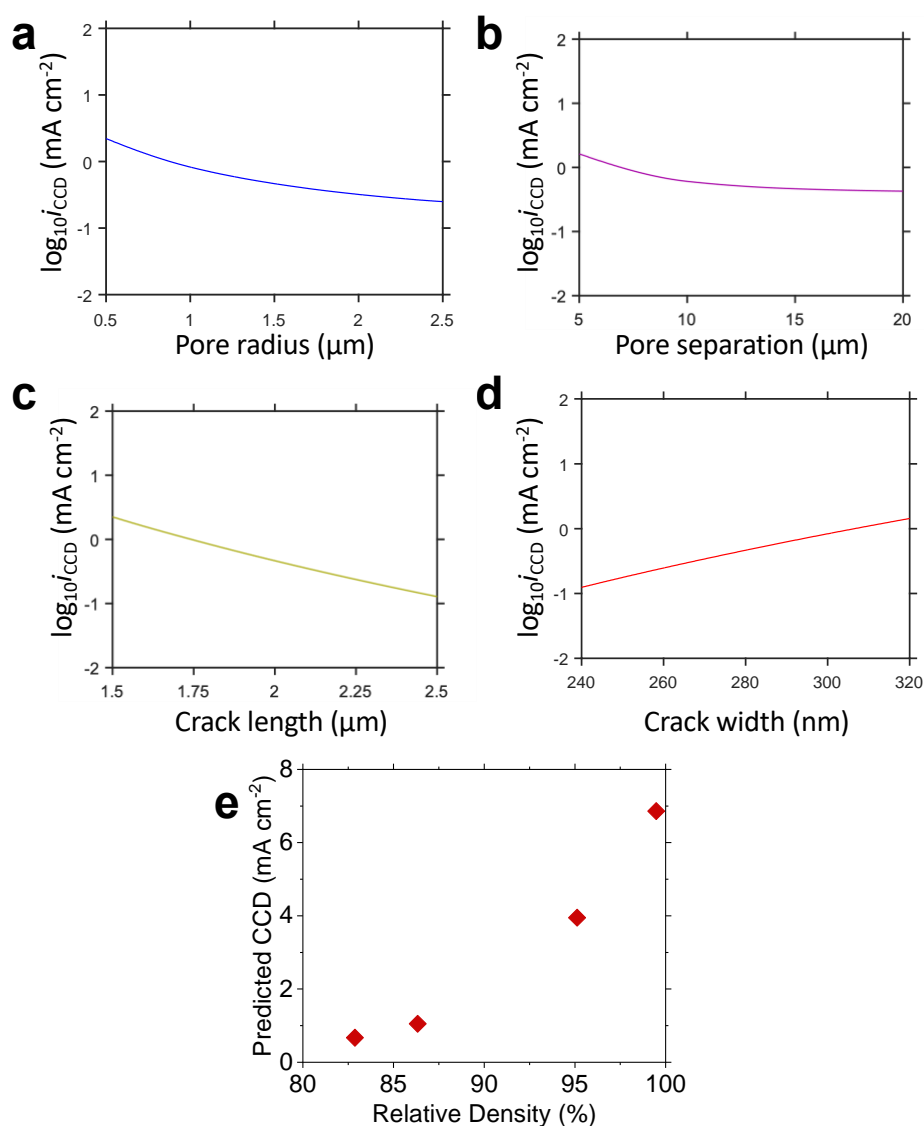

Figure 5. Effect of pore size and separation as well as crack length and width on the CCD calculated using the dendrite model. The combined effect of the changes in the

four parameters is reflected in the CCD predictions. The effect on the critical current density for dendrite initiation of, **a,** pore radius, **b,** pore separation, **c,** crack length and **d** crack width. **e** Plot of predicted overall CCDs for each density of Li_6PS_5Cl.

The high CCD of 10 mA cm^{-2} for the 99% densified solid electrolyte, Fig 1, enables extended cycling without short-circuit at high, practical, plating current densities. This is illustrated in Fig 6, where three electrode cells with a lithium working electrode are plated at a current density of 9 mA cm^{-2}. In the case of the 83% dense (cold pressed) Li_6PS_5Cl solid electrolyte the cell short-circuits after 6 cycles. Whereas the 99% dense Li_6PS_5Cl solid electrolyte cycled continuously until the cycling was stopped after 100 cycles. In both cases stripping was carried out at the lower current density of 0.05 mA cm^{-2} to avoid voiding at the interface. It is worth noting that even the 99% dense Li_6PS_5Cl discs retain surface roughness, as shown by the AFM scans in Fig S9, and it is not necessary to strip first in order to create defects for dendrites to grow on plating. The mechanism of dendrite formation is the same across the densities studied. As the focus of this paper is the effect of densification on dendrite suppression on plating and not on voiding, when stripping we used a 7 MPa stack pressure along with the 0.05 mA cm^{-2} stripping current mentioned above to prevent voiding formation. The sustained cyclability of the 99% dense solid electrolyte is not related to any suppression of dendrite propagation after initiation. As shown by the XCT images in Fig 2, there are no dendrites at this plating current density.
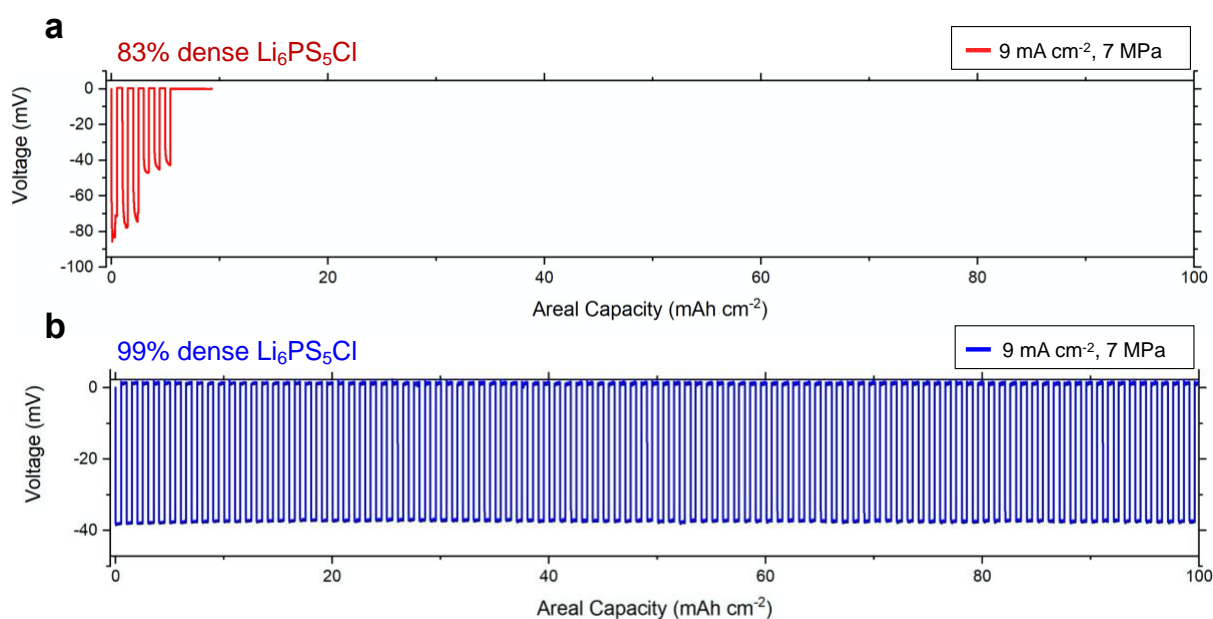

Figure 6. Repeated fast plating at 9 mA cm^{-2} enabled by densifying the Li_6PS_5Cl microstructure. Cycling of Li/Li_6PS_5Cl 3-electrode cells with current densities of 9 mA cm^{-2} for plating, 0.05 mA cm^{-2} for stripping (to avoid void formation), both for a capacity of 0.5 mAh cm^{-2}, under 7 MPa stack pressure, with **a,** a cold pressed Li_6PS_5Cl disc (83% dense) and **b,** a 400°C sintered Li_6PS_5Cl disc (99% dense).

As mentioned above and noted previously, although Li_6PS_5Cl reacts with Li metal, it does so to form a solid electrolyte interphase that stabilises with time[62,70,71]. This was seen to be consistent regardless of density, see Fig S10. The cells were always rested to allow stabilisation. This reacted interphase layer is typically thin (< 250 nm), meaning its effect on dendrite initiation is minimal[62]. The interphase is also stable during cycling, see Figure S11.

Implications

Sintering Argyrodite, Li_6PS_5Cl, solid electrolytes to a density of 99% results in a critical current for lithium dendrites of 10 mA cm^{-2}. Plating lithium at the solid electrolyte interface at a current density of 9 mA cm^{-2} shows no evidence of lithium dendrites electrochemically or in X-ray CT imaging. The early motivation to develop ceramic electrolyte batteries was based on the belief that dense ceramics would not permit Li dendrites to form and short-circuit cells. Yet, previous studies have suggested that dense ceramics, even with 99% density, do not guarantee Li plating at practical currents[30,31]. Critical currents are often limited to a few mA cm^{-2}. The results here show that not all the changes in microstructure on densification necessarily favour increased CCDs. Densification decreases crack width and increasing pore separation, which act to decrease CCD, while the decreasing crack length and smaller pores act to increase CCD. For Li_6PS_5Cl, the latter outweigh the former. The high degree of densification is achieved here by spark plasma sintering. A future challenge is to achieve high degrees of densification by more scalable routes. Also, different densification protocols are known to result in different microstructures of polycrystalline ceramics[72–75]. The results reported here inspire investigation of other densification methods directed to optimising the microstructural parameters that increase CCD, such as small pores, while suppressing those that act to decrease CCD, such as narrow cracks. Our results also highlight the need to study microstructure and CCD relations across a range material systems. Future work focussed on scalable sintering of sulphide electrolytes may enable practical charging rates for solid state cells employing lithium anodes without the need to form composite electrolytes or use interlayers.

Author Contributions:

D.L.R.M. contributed to all aspects of the research. D.L.R.M., D.S.J., B.H, S.Z., Z.N., and S.M. carried out the in-situ synchrotron XCT. D.L.R.M. performed the preparation of electrolyte discs and cell assembly. D.L.R.M, Z.N., and J.B., optimised the sintering conditions for the electrolyte. D.L.R.M. and Z.N. performed the powder X-ray Diffraction. G.J.R performed the Raman spectroscopy. M.S., and D.L.R.M performed the Plasma FIB imaging. G.L. conducted the modelling. D.L.R.M., G.L., D.S.J., M.S., P.S.G., T.J.M., and P.G.B. discussed the data. All authors contributed to the interpretation of data. D.L.R.M., G.L., D.S.J. and P.G.B. wrote the manuscript with contributions and revisions from all authors. The project was supervised by D.S.J. and P.G.B.

References

1. Janek, J. & Zeier, W. G. A solid future for battery development. *Nat. Energy* **1**, 16141 (2016).

2. Liu, J. *et al.* Pathways for practical high-energy long-cycling lithium metal batteries. *Nat. Energy* **4**, 180–186 (2019).
3. Famprikis, T., Canepa, P., Dawson, J. A., Islam, M. S. & Masquelier, C. Fundamentals of inorganic solid-state electrolytes for batteries. *Nat. Mater.* **18**, 1278–1291 (2019).
4. McConohy, G. *et al.* Mechanical regulation of lithium intrusion probability in garnet solid electrolytes. *Nat. Energy* **8**, 241–250 (2023).
5. Singh, D. K. *et al.* Li6PS5Cl microstructure and influence on dendrite growth in solid-state batteries with lithium metal anode. *Cell Rep. Phys. Sci.* **3**, 101043 (2022).
6. Singh, D. K., Fuchs, T., Krempaszky, C., Mogwitz, B. & Janek, J. Non-Linear Kinetics of The Lithium Metal Anode on Li6PS5Cl at High Current Density: Dendrite Growth and the Role of Lithium Microstructure on Creep. *Adv. Sci.* **n/a**, 2302521 (2023).
7. Cho, J. H. *et al.* An Investigation of Chemo-Mechanical Phenomena and Li Metal Penetration in All-Solid-State Lithium Metal Batteries Using In Situ Optical Curvature Measurements. *Adv. Energy Mater.* **12**, 2200369 (2022).
8. Barroso-Luque, L., Tu, Q. & Ceder, G. An Analysis of Solid-State Electrodeposition-Induced Metal Plastic Flow and Predictions of Stress States in Solid Ionic Conductor Defects. *J. Electrochem. Soc.* **167**, 20534 (2020).
9. Tu, Q., Shi, T., Chakravarthy, S. & Ceder, G. Understanding metal propagation in solid electrolytes due to mixed ionic-electronic conduction. *Matter* **4**, 3248–3268 (2021).
10. Cheng, L. *et al.* Effect of Surface Microstructure on Electrochemical Performance of Garnet Solid Electrolytes. *ACS Appl. Mater. Interfaces* **7**, 2073–2081 (2015).
11. Geng, L. *et al.* Morphodynamics of dendrite growth in alumina based all solid-state sodium metal batteries. *Energy Environ. Sci.* **16**, 2658–2668 (2023).
12. Ning, Z. *et al.* Dendrite initiation and propagation in lithium metal solid-state batteries. *Nature* **618**, 287–293 (2023).
13. Ning, Z. *et al.* Visualizing plating-induced cracking in lithium-anode solid-electrolyte cells. *Nat. Mater.* **20**, 1121–1129 (2021).
14. Kazyak, E. *et al.* Li Penetration in Ceramic Solid Electrolytes: Operando Microscopy Analysis of Morphology, Propagation, and Reversibility. *Matter* **2**, 1025–1048 (2020).
15. Fincher, C. D. *et al.* Controlling dendrite propagation in solid-state batteries with engineered stress. **12**, (2022).
16. Liu, X. *et al.* Local electronic structure variation resulting in Li 'filament' formation within solid electrolytes. *Nat. Mater.* **20**, 1485–1490 (2021).
17. Han, F. *et al.* High electronic conductivity as the origin of lithium dendrite formation within solid electrolytes. *Nat. Energy* **4**, 187–196 (2019).
18. Fu, C. *et al.* Universal chemomechanical design rules for solid-ion conductors to prevent dendrite formation in lithium metal batteries. *Nat. Mater.* **19**, 758–766 (2020).
19. Wan, H. *et al.* Critical interphase overpotential as a lithium dendrite-suppression criterion for all-solid-state lithium battery design. *Nat. Energy* **8**, 473–481 (2023).
20. Dixit, M. B. *et al.* Polymorphism of garnet solid electrolytes and its implications for grain-level chemo-mechanics. *Nat. Mater.* **21**, 1298–1305 (2022).
21. Lewis, J. A. *et al.* Linking void and interphase evolution to electrochemistry in solid-state batteries using operando X-ray tomography. *Nat. Mater.* **20**, 503–510 (2021).
22. Liang, Z. *et al.* Understanding the failure process of sulfide-based all-solid-state lithium batteries via operando nuclear magnetic resonance spectroscopy. *Nat. Commun.* **14**, 259 (2023).
23. Wang, M. J., Kazyak, E., Dasgupta, N. P. & Sakamoto, J. Transitioning solid-state batteries from lab to market: Linking electro-chemo-mechanics with practical considerations. *Joule* **5**, 1371–1390 (2021).
24. Janek, J. & Zeier, W. G. Challenges in speeding up solid-state battery development. *Nat. Energy* **8**, 230–240 (2023).
25. Kasemchainan, J. *et al.* Critical stripping current leads to dendrite formation on plating in lithium anode solid electrolyte cells. *Nat. Mater.* **18**, (2019).
26. Ham, S.-Y. *et al.* Assessing the critical current density of all-solid-state Li metal symmetric and full cells. *Energy Storage Mater.* **55**, 455–462 (2023).
27. Zhu, C. *et al.* Understanding the evolution of lithium dendrites at Li6.25Al0.25La3Zr2O12 grain boundaries via operando microscopy techniques. *Nat. Commun.* **14**, 1300 (2023).

28. Zhou, L. *et al.* High areal capacity, long cycle life 4 V ceramic all-solid-state Li-ion batteries enabled by chloride solid electrolytes. *Nat. Energy* **7**, 83–93 (2022).

29. Yin, Y.-C. *et al.* A LaCl3-based lithium superionic conductor compatible with lithium metal. *Nature* **616**, 77–83 (2023).

30. Reisecker, V. *et al.* Effect of pulse-current-based protocols on the lithium dendrite formation and evolution in all-solid-state batteries. *Nat. Commun.* **14**, 2432 (2023).

31. Fuchs, T., Haslam, C. G., Richter, F. H., Sakamoto, J. & Janek, J. Evaluating the Use of Critical Current Density Tests of Symmetric Lithium Transference Cells with Solid Electrolytes. *Adv. Energy Mater.* **13**, 2302383 (2023).

32. Shen, F., Dixit, M. B., Xiao, X. & Hatzell, K. B. Effect of Pore Connectivity on Li Dendrite Propagation within LLZO Electrolytes Observed with Synchrotron X-ray Tomography. *ACS Energy Lett.* **3**, 1056–1061 (2018).

33. Lee, Y.-G. *et al.* High-energy long-cycling all-solid-state lithium metal batteries enabled by silver–carbon composite anodes. *Nat. Energy* **5**, 299–308 (2020).

34. Spencer-Jolly, D. *et al.* Structural changes in the silver-carbon composite anode interlayer of solid-state batteries. *Joule* **7**, 503–514 (2023).

35. Kim, N. *et al.* Carbide-mediated catalytic hydrogenolysis: defects in graphene on a carbonaceous lithium host for liquid and all-solid-state lithium metal batteries. *Energy Environ. Sci.* **16**, 2505–2517 (2023).

36. Chen, Y. *et al.* Li metal deposition and stripping in a solid-state battery via Coble creep. *Nature* **578**, 251–255 (2020).

37. Deng, T. *et al.* Tuning the Anode–Electrolyte Interface Chemistry for Garnet-Based Solid-State Li Metal Batteries. *Adv. Mater.* **32**, 2000030 (2020).

38. Negating interfacial impedance in garnet-based solid-state Li metal batteries. *Nat Mater* **16**, 572 (2017).

39. Feng, W. *et al.* Stabilization of garnet/Li interphase by diluting the electronic conductor. *Sci. Adv.* **8**, eadd8972 (2023).

40. Landgraf, V. *et al.* Li5NCl2: A Fully-Reduced, Highly-Disordered Nitride-Halide Electrolyte for Solid-State Batteries with Lithium-Metal Anodes. *ACS Appl. Energy Mater.* **6**, 1661–1672 (2023).

41. Inaoka, T. *et al.* Tin Interlayer at the Li/Li3PS4 Interface for Improved Li Stripping/Plating Performance. *J. Phys. Chem. C* **127**, 10453–10458 (2023).

42. Park, R. J.-Y. *et al.* Semi-solid alkali metal electrodes enabling high critical current densities in solid electrolyte batteries. *Nat. Energy* **6**, 314–322 (2021).

43. Peng, J. *et al.* High Current Density and Long Cycle Life Enabled by Sulfide Solid Electrolyte and Dendrite-Free Liquid Lithium Anode. *Adv. Funct. Mater.* **32**, 2105776 (2022).

44. Contact between garnet-type solid electrolyte and lithium metal anode: influence on charge transfer resistance and short circuit prevention. *J Electrochem Soc* **164**, A666 (2017).

45. Xu, R. *et al.* A Morphologically Stable Li/Electrolyte Interface for All-Solid-State Batteries Enabled by 3D-Micropatterned Garnet. *Adv. Mater.* **33**, 2104009 (2021).

46. Xu, S. *et al.* Three-Dimensional, Solid-State Mixed Electron–Ion Conductive Framework for Lithium Metal Anode. *Nano Lett.* **18**, 3926–3933 (2018).

47. Yersak, T., Salvador, J. R., Schmidt, R. D. & Cai, M. Hot Pressed, Fiber-Reinforced (Li2S)70(P2S5)30 Solid-State Electrolyte Separators for Li Metal Batteries. *ACS Appl. Energy Mater.* **2**, 3523–3531 (2019).

48. Wang, S. *et al.* High-conductivity free-standing Li6PS5Cl/poly(vinylidene difluoride) composite solid electrolyte membranes for lithium-ion batteries. *J. Materiomics* **6**, 70–76 (2020).

49. Ye, L. & Li, X. A dynamic stability design strategy for lithium metal solid state batteries. *Nature* **593**, 218–222 (2021).

50. Pervez, S. A. *et al.* Fabrication of a Dendrite-Free all Solid-State Li Metal Battery via Polymer Composite/Garnet/Polymer Composite Layered Electrolyte. *Adv. Mater. Interfaces* **6**, 1900186 (2019).

51. Porz, L. *et al.* Mechanism of Lithium Metal Penetration through Inorganic Solid Electrolytes. *Adv. Energy Mater.* **7**, 1–12 (2017).

52. Swamy, T. *et al.* Lithium Metal Penetration Induced by Electrodeposition through Solid Electrolytes: Example in Single-Crystal Li 6 La 3 ZrTaO 12 Garnet . *J. Electrochem. Soc.* **165**, A3648–A3655 (2018).

53. Krauskopf, T. *et al.* The Fast Charge Transfer Kinetics of the Lithium Metal Anode on the Garnet-Type Solid Electrolyte Li6.25Al0.25La3Zr2O12. *Adv. Energy Mater.* **10**, 2000945 (2020).

54. Yersak, T. A., Salvador, J. R., Pieczonka, N. P. W. & Cai, M. Dense, Melt Cast Sulfide Glass Electrolyte Separators for Li Metal Batteries. *J. Electrochem. Soc.* **166**, A1535 (2019).

55. Garcia-Mendez, R., Mizuno, F., Zhang, R., Arthur, T. S. & Sakamoto, J. Effect of Processing Conditions of 75Li2S-25P2S5 Solid Electrolyte on its DC Electrochemical Behavior. *Electrochimica Acta* **237**, 144–151 (2017).

56. Garcia-Mendez, R., Smith, J. G., Neuefeind, J. C., Siegel, D. J. & Sakamoto, J. Correlating Macro and Atomic Structure with Elastic Properties and Ionic Transport of Glassy Li 2 S-P 2 S 5 (LPS) Solid Electrolyte for Solid-State Li Metal Batteries . *Adv. Energy Mater.* **5**, 2000335 (2020).

57. Asakura, T. *et al.* Stack Pressure Dependence of Li Stripping/Plating Performance in All-Solid-State Li Metal Cells Containing Sulfide Glass Electrolytes. *ACS Appl. Mater. Interfaces* **15**, 31403–31408 (2023).

58. McGrogan, F. P. *et al.* Compliant Yet Brittle Mechanical Behavior of Li2S–P2S5 Lithium-Ion-Conducting Solid Electrolyte. *Adv. Energy Mater.* **7**, 1602011 (2017).

59. Bates, J. B., Dudney, N. J., Neudecker, B., Ueda, A. & Evans, C. D. Thin-film lithium and lithium-ion batteries. *Solid State Ion.* **135**, 33–45 (2000).

60. López-Aranguren, P. *et al.* Crystalline LiPON as a Bulk-Type Solid Electrolyte. *ACS Energy Lett.* **6**, 445–450 (2021).

61. Kato, Y. *et al.* High-power all-solid-state batteries using sulfide superionic conductors. *Nat. Energy* **1**, 1–7 (2016).

62. Otto, S.-K. *et al.* In Situ Investigation of Lithium Metal–Solid Electrolyte Anode Interfaces with ToF-SIMS. *Adv. Mater. Interfaces* **9**, 2102387 (2022).

63. Lewis, J. A. *et al.* Role of Areal Capacity in Determining Short Circuiting of Sulfide-Based Solid-State Batteries. *ACS Appl. Mater. Interfaces* **14**, 4051–4060 (2022).

64. Doux, J.-M. *et al.* Stack Pressure Considerations for Room-Temperature All-Solid-State Lithium Metal Batteries. *Adv. Energy Mater.* **10**, 1903253 (2020).

65. Kato, A., Yamamoto, M., Sakuda, A., Hayashi, A. & Tatsumisago, M. Mechanical Properties of Li2S–P2S5 Glasses with Lithium Halides and Application in All-Solid-State Batteries. *ACS Appl. Energy Mater.* **1**, 1002–1007 (2018).

66. Hikima, K., Totani, M., Obokata, S., Muto, H. & Matsuda, A. Mechanical Properties of Sulfide-Type Solid Electrolytes Analyzed by Indentation Methods. *ACS Appl. Energy Mater.* **5**, 2349–2355 (2022).

67. Wang, A.-N. *et al.* Mechanical properties of the solid electrolyte Al-substituted Li7La3Zr2O12 (LLZO) by utilizing micro-pillar indentation splitting test. *J. Eur. Ceram. Soc.* **38**, 3201–3209 (2018).

68. Wolfenstine, J., Allen, J. L., Sakamoto, J., Siegel, D. J. & Choe, H. Mechanical behavior of Li-ion-conducting crystalline oxide-based solid electrolytes: a brief review. *Ionics* **24**, 1271–1276 (2018).

69. Ni, J. E., Case, E. D., Sakamoto, J. S., Rangasamy, E. & Wolfenstine, J. B. Room temperature elastic moduli and Vickers hardness of hot-pressed LLZO cubic garnet. *J. Mater. Sci.* **47**, 7978–7985 (2012).

70. Wenzel, S., Sedlmaier, S. J., Dietrich, C., Zeier, W. G. & Janek, J. Interfacial reactivity and interphase growth of argyrodite solid electrolytes at lithium metal electrodes. *Solid State Ion.* **318**, 102–112 (2018).

71. Narayanan, S. *et al.* Effect of current density on the solid electrolyte interphase formation at the lithium|Li6PS5Cl interface. *Nat. Commun.* **13**, 7237 (2022).

72. Lian, J. *et al.* Influence of Cooling Rates on the Microstructure and Mechanical Properties of Aluminum Titanate Flexible Ceramic. *Adv. Eng. Mater.* **23**, 2100170 (2021).

73. Shojai, F. & Mäntylä, T. A. Effect of sintering temperature and holding time on the properties of 3Y-ZrO2 microfiltration membranes. *J. Mater. Sci.* **36**, 3437–3446 (2001).

74. Varela, J. A., Whittemore, O. J. & Longo, E. Pore size evolution during sintering of ceramic oxides. *Ceram. Int.* **16**, 177–189 (1990).
75. Lóh, N. J., Simão, L., Faller, C. A., De Noni, A. & Montedo, O. R. K. A review of two-step sintering for ceramics. *Ceram. Int.* **42**, 12556–12572 (2016).

Methods

Spark plasma sintering and electrolyte preparation

All procedures were performed in an Ar-filled glovebox (O_2 and H_2O levels < 1 ppm). Li_6PS_5Cl powder was purchased from Ampcera (SEM of as-received power shown in Fig S12) and measurements were performed to verify the absence of any carbon impurities, see Figure S13. The powder was loaded into a graphite die set which was then inserted into a spark plasma sintering system (FCT systeme GmbH) within an Ar-filled glovebox and subject to 50 MPa uniaxial pressure at either 300 °C, 350 °C or 400 °C for 5 minutes while under vacuum by passing a current through the die set. 5-mm diameter sintered electrolyte discs of identical thickness (1 mm) were then used for cell assembly. EIS measurements confirm an increase in conductivity with densification, Fig S14, consisted with lower grain boundary resistances on densification. Cold pressed electrolyte discs were formed by loading the same pristine electrolyte powder into a 5-mm-diameter stainless-steel die set and pressing under a uniaxial pressure of 400 MPa. To determine the relative density of the electrolytes, discs were weighed, and their total volume measured using micro-XCT.

Three-electrode cells

For a three-electrode cell, two disc-shaped lithium electrodes of 1 mm diameter were pressed onto the same side of the electrolyte disc as the working and reference electrodes respectively. The remaining areas of the electrolyte surface were then covered by insulating polymer tape. A 5-mm lithium disc was pressed onto the opposite side as the counter electrode. The assembly was placed into a pouch cell and sealed under vacuum. A stack pressure of 7 MPa was applied to all cells in this study. For CCD determination, cells were subject to galvanostatic single plating for a capacity of 8 mAh cm^{-2}. For cycling studies, cells were cycled galvanostatically with a capacity on each half-cycle of 0.5 mAh cm^{-2}. Although the plating current on the working electrode was 9.0 mA cm^{-2}, a current density of 0.05 mA cm^{-2} was used on stripping to avoid void formation at the working electrode–solid electrolyte interface. All galvanostatic measurements were performed using a Gamry Interface 1010 potentiostat.

Potentiostatic EIS

PEIS was taken using a 5 mV voltage perturbation, collecting 10 points per decade across a frequency range of 1 MHz – 1 Hz. PEIS data were analysed and fitted by equivalent circuit models using the ZView software package.

In-situ X-ray Tomography

X-ray tomograms were recorded at the I13-2 beamline at the Diamond Light Source and the TOMCAT beamline at the Swiss Light Source (Paul Scherrer Institute). For both experiments the projections were collected with a PCO pco.edge 5.5 sCMOS camera combined with an optical microscope with a 4× magnification, resulting in a pixel size of 1.63 µm. For each tomogram, 1,801 equiangularly distributed projections were taken over 180°. Additionally, X-

ray tomograms were collected using a Zeiss Xradia 610 Versa X-ray microscope and 3201 equiangularly distributed projections were taken over 360° for each tomogram, with a resultant pixel size of 1.63 μm. For the in-situ measurements, metallic lithium foil was punched into disc-shaped lithium electrodes and pressed onto both sides of the electrolyte disc, 1 mm diameter electrodes were used for the working electrode and 3 mm for the counter. X-ray tomograms were obtained at the pristine state and after charging in successive steps of 0.1 mAh cm^{-2}. During the experiment, 7 MPa of pressure was applied using a constantly applied spring force, which was measured and calibrated using a transducer.

Plasma FIB-SEM and microstructure analysis

Solid electrolyte discs were transferred into the chamber of a plasma FIB scanning electron microscope (Helios G4 PFIB DualBeam, Thermo Fisher Scientific) for FIB milling with an iLoad vacuum sample transfer system without exposure to air. The freshly milled cross-section was then imaged with the SEM to visualize the pores and cracks in proximity to the interface. Automated serial sectioning was used to obtain a three-dimensional depiction of the porosity. A 30 kV and 15 nA Xe+ beam was used to mill the volume of interest and capture a stack of secondary electron cross-sectional images. Each slice had a thickness of 100 nm. To construct a three-dimensional view, the sequence of 2D secondary electron images were aligned using Avizo 3D (version 2021.2, ThermoFisher Scientific). Using the Avizo 3D software the images were subjected to a semi-automated segmentation process to differentiate between pores, cracks, and bulk electrolyte. The dimensions of the largest pores and longest cracks were obtained from the segmentation analysis and used as inputs for the modelling simulations.

Powder XRD

The electrolyte discs were ground into powders using a pestle and mortar. X-ray diffraction was performed using a Rigaku MiniFlex 600 instrument located within a nitrogen glovebox.